buildings

MDPI

Article

Influence of Friction Models on the Seismic Response of Box-Girder RC Bridges with Double Concave Friction Pendulum Bearings Under Varying Deck Aspect and Mass Ratios

Muzaffer Borekci

Department of Civil Engineering, Yildiz Technical University, Istanbul 34220, Turkey; mborekci@yildiz.edu.tr

Abstract: Friction pendulum bearings are widely used seismic isolation devices for bridges, with their behavior governed by friction during excitation. Sliding velocity and contact pressure are among the factors that substantially affect the friction coefficient. Common friction models include the Coulomb model, which assumes constant friction and neglects both sliding velocity and contact pressure, and the velocity-dependent model, which ignores contact pressure. This study investigates the impact of neglecting contact pressure on bridge response by additionally employing a velocity-pressure-dependent friction model and comparing the effects of these three models on the bridge response. Five 3-span box-girder RC bridges were modeled in OpenSees (v3.5.0) using Coulomb, velocity-dependent, and velocity-pressure-dependent friction models. Deck height variations were introduced to account for axial load changes on bearings. Nonlinear time history analyses were performed to evaluate seismic responses. The study also explored the effects of substructure-to-superstructure mass ratio and variations in the experimentally obtained rate parameter of velocity-dependent and velocity-pressure-dependent models. Results indicate that the velocity-pressure-dependent model provides more consistent predictions, while the rate parameter has negligible effects. The velocity-pressure-dependent model increases isolator displacement by nearly 2.5 times compared to the Coulomb and velocity-dependent models. Differences in responses are influenced more by the mass ratio than by the deck aspect ratio.

Keywords: box-girder bridges; friction pendulum; friction model; contact pressure; deck aspect ratio; nonlinear dynamic analysis

check for updates

Academic Editor: Weixin Ren

Received: 17 January 2025
Revised: 6 February 2025
Accepted: 10 February 2025
Published: 12 February 2025

Citation: Borekci, M. Influence of Friction Models on the Seismic Response of Box-Girder RC Bridges with Double Concave Friction Pendulum Bearings Under Varying Deck Aspect and Mass Ratios. *Buildings* **2025**, *15*, 556. https://doi.org/10.3390/buildings15040556

Copyright: © 2025 by the author. Licensee MDPI, Basel, Switzerland. This article is an open access article distributed under the terms and conditions of the Creative Commons Attribution (CC BY) license (https://creativecommons.org/licenses/by/4.0/).

1. Introduction

Bridges are crucial for transportation, especially following severe earthquakes, and must remain functional in their aftermath. To ensure this, a high level of seismic performance is essential. The required high seismic performance level can effectively be satisfied by utilizing seismic isolators between the bridge deck and the pier, which decouple the superstructure—a large mass—from horizontal ground motion. Friction pendulum bearings (FPBs) are among the most commonly used isolation devices for bridges, as reported in the literature [1–5]. These devices dissipate energy through the friction generated between the articulated slider and the concave sliding surfaces. Consequently, the behavior of an FPB is primarily governed by friction, adding complexity to its performance [6].

Due to their vital post-earthquake role, not only the bridge but also its bearings must be accurately modeled. When FPBs are used as bearings, developing a reliable analytical model for them in bridges requires precise assumptions about friction and dependable modeling

methods. Many studies have investigated the friction coefficient of FPBs and its dependent parameters. Apart from various factors such as environmental conditions and the inherent properties of materials, as detailed in the study by Constantinou et al. [7], the friction coefficient of an FPB primarily depends on the sliding velocity, temperature, and the apparent contact pressure between the articulated slider and the concave surface [8–12]. Friction in sliding isolators and the parameters influencing it are comprehensively discussed in the following section.

Despite its dependency on sliding velocity, temperature, and contact pressure, a constant friction coefficient, commonly known as Coulomb friction, is often used in modeling due to its simplicity and convenience [13–15]. Another commonly used friction model in the literature is the velocity-dependent model, which accounts for the effects of sliding velocity on the friction coefficient. This model is implemented in several analytical modeling programs, such as SAP2000 [16] and OpenSees [17]. During a seismic event, sliding velocity significantly influences the system, making it a critical factor in friction behavior. Due to its relevance, the velocity-dependent friction model was adopted for this study [18–21].

Another parameter that affects friction is contact pressure, or in other words, the axial load on the bearing. While its significant influence on the friction coefficient has been highlighted in several studies [7,12,22], incorporating pressure-dependent effects, i.e., axial load, into analytical modeling of bridges is not a common practice. Given the variation in axial load on bearings due to overturning effects induced by lateral forces, a pressure-dependent friction model could have a substantial impact on the seismic behavior of both the bearing and the bridge [6]. This effect becomes particularly significant in bridges with high ratios of deck center-of-mass height to the distance between bearings [23].

To date, there is a noticeable lack of documented studies in the literature exploring the impact of pressure-dependent friction models on the seismic behavior of bridges. Calvi et al. [23] investigated the effects of axial load variation on the seismic response of bridges with FPBs using single-pier models for variable aspect ratios (ARs), defined as the ratio between the relative distance between two bearings and the vertical distance from the center of gravity of the deck mass to the FPB base. Nonlinear time history analyses were performed with five ground motion records, each comprising three components. The structural system included the foundation, pier, isolation devices, and deck section. All elements were modeled with linear elastic behavior, except for the isolators, which were represented as nonlinear radial elements. While the study assumed a constant friction coefficient of 5%, the yielding level and post-yield stiffness in the nonlinear phase of the hysteretic response were adjusted to account for axial load variations. The findings revealed that including axial force effects may not significantly impact displacement demand but can result in notable increases in shear, bending, and torsional moment demands on the piers. However, the study's results are based on a parametric analytical model that excludes bending–shear–torsion interaction. Incorporating these interactions into analytical models is now feasible with the capabilities of modern high-performance computational programs.

This study aims to investigate both the effects of different friction models and neglecting contact pressure in the friction model on the seismic response of bridges, considering axial load variations on the bearings. For this purpose, five distinct 3-span box-girder RC bridges with two-column piers were analyzed. The bridges differ in their deck height, allowing for variations in the center of gravity of the deck mass and, consequently, the aspect ratio (AR). Six different ARs, ranging from 4 to 9, were considered, while all other dimensions, including the distance between bearings, remained constant. A double pendulum bearing (DPB) was used as the seismic isolator. Notably, equations of velocity-dependent and velocity-pressure-dependent friction models considered in this study include a rate parameter (explained in the following section) that requires experimental estimation. This pa-

rameter primarily depends on both the material of the contact surfaces and contact pressure. The study also examined how variations in this parameter affect the influence of velocity-dependent and velocity-pressure-dependent friction models on bridge response. To isolate this effect, material and pressure were not considered, allowing for an investigation of how the rate parameter impacts the overall behavior of isolators and bridges. To achieve the study's objectives, the bridges were modeled in OpenSees (v3.5.0) [17] using the spine model assumption with Coulomb, velocity-dependent and velocity-pressure-dependent friction model assumptions available in the OpenSees (v3.5.0) [17] library. Nonlinear time history analyses were conducted for 11 pairs of ground motions scaled to a target spectrum. Additionally, as changes in AR alter the ratio of substructure mass to superstructure mass, the relationship between this mass ratio and the influence of velocity-dependent and velocity-pressure-dependent friction models on bridge response was investigated to determine whether AR plays a significant role in the observed effects. Considering that even the most important and widely used seismic design guidelines, such as ASCE/SEI 7-22 [24], AASHTO (2014) [25], and EN 15129:2018 [26], suggest accounting for sliding velocity in friction coefficient modeling without considering the effect of contact pressure, the results obtained from this study will be highly significant.

2. Friction in Sliding Bearings

Friction controls the behavior of sliding bearings by dissipating seismic energy through sliding interface interactions and reducing lateral stiffness. Although the friction coefficient can be influenced by environmental factors such as contamination and corrosion, it is predominantly governed by inherent parameters, including sliding velocity and axial pressure, which are unavoidable in practice. Two types of friction emerge in sliding bearings during seismic loading: breakaway (static) and sliding (dynamic) friction. Breakaway friction represents the maximum force that must be overcome to initiate movement. Once the object begins to move, it transitions from breakaway friction to sliding friction, which occurs when two surfaces are in relative motion. After the breakaway friction is overcome, the friction coefficient generally drops to a minimum value (f_{min}) at slow velocities and increases with increasing velocity, attaining a constant maximum value (f_{max}) at large velocities. The relation between the coefficient of friction and velocity is represented in Figure 1, along with the relation to axial load.

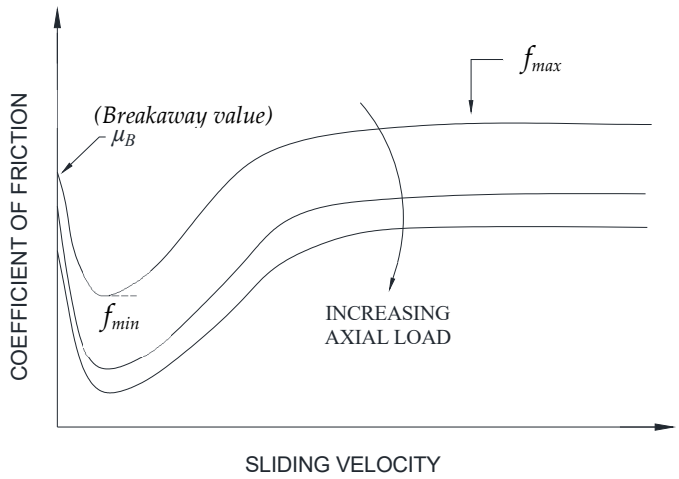


Figure 1. Coefficient of friction dependency on sliding velocity and normal load [7].

Mokha et al. [9,27] and Constantinou et al. [8] reported that for PTFE interfaces with unfilled and glass-filled materials, the μ_B/f_{min} ratio at 20 °C ranges from 1.3 to 4.4. According to the experiments of Campbell et al. [28], this ratio varies approximately between 2 and 7

for various PTFE interfaces. In contrast, Mokha et al. [9] and Campbell et al. [28] indicate that for woven PTFE, the μ_B/f_{min} ratio lies between 2 and 3. For FPBs with filled PTFE-polished stainless-steel surfaces, the μ_B/f_{min} ratio is generally around 1.20 [7]. Constantinou et al. [29] and Tsopelas et al. [30] further demonstrated through their experiments that the friction coefficient at high velocities (f_{max}) is greater than the static friction coefficient (μ_B).

Temperature significantly affects breakaway friction and sliding friction at very low velocities. However, its effect on sliding friction at high velocities is negligible due to frictional heating [28]. Tests in the literature have shown that the friction coefficient decreases with increasing temperature [7]. Note that in this study, the effect of temperature on friction is neglected despite its influence, and a standard temperature is assumed for friction calculations. An equation for the sliding friction coefficient was proposed by Mokha et al. [27] and Constantinou et al. [8] for constant apparent pressure, and this relation is given in Equation (1). In this equation, α describes the transition rate parameter from f_{min} to f_{max} for constant pressure, while V stands for sliding velocity.

$$\mu = f_{max} - (f_{max} - f_{min})e^{(-\alpha V)} \quad (1)$$

Mokha et al. [31] suggested a rate parameter (α) for unfilled Teflon to be 15.75 s/m and 17.72 s/m in the parallel and perpendicular directions, respectively. These values were provided for 3.45 MPa pressure on the specimens. Additionally, Constantinou et al. [29] performed several tests on an FPB with four different materials at the sliding interface and obtained rate parameters ranging from 47 to 83.4 s/m for 17.2 MPa apparent pressure and 199.7 s/m for 275.6 MPa apparent pressure. α ranges from 20 to 30 s/m for unfilled PTFE, whereas it is about 100 s/m or larger for filled PTFE [32]. Moreover, Dao et al. [33] conducted shake table tests on a full-scale building isolated with Triple Pendulum Bearings (TPBs) at E-Defence. They suggested a rate parameter value of 54.41 s/m based on the data obtained from the tests. The literature suggests different rate parameters for various materials at the sliding interface, ranging from 15 to 200.

Another key parameter influencing the friction coefficient is contact pressure, as shown in Figure 1, where an increase in pressure corresponds to a decrease in the friction coefficient [9,32,34]. 'Contact' refers to the sum of the areas of all junctions in the sliding interface, which represents the real area of contact used to estimate pressure. In contrast, the geometric contact area between the concave plate and the slider is the apparent area, which is significantly larger than the actual contact area, particularly for bimetallic interfaces. However, for FPBs, pressure can be estimated using the apparent area since PTFE, being much softer than steel, is compressed by the larger rigid stainless-steel plate [7]. A view of a double concave surface FPB and the definition of contact area types are illustrated in Figure 2.

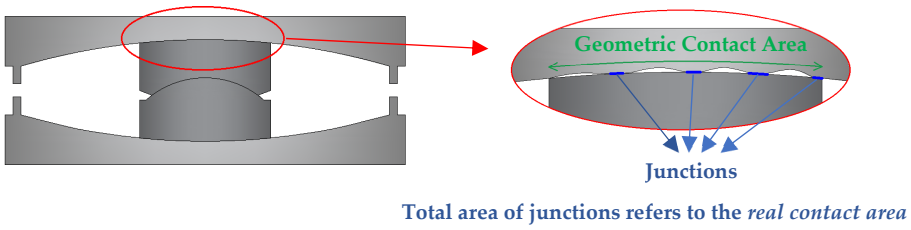


Figure 2. Schematic view of a double concave surface FPB and the definition of contact area.

Constantinou et al. [29] and Tsopelas et al. [30] proposed a modification for f_{max} given in Equation (1) to incorporate the pressure effect on friction coefficient as in Equation (2).

$$f_{max} = f_{max0} - \Delta f.tanh(\gamma p) \quad (2)$$

In Equation (2), f_{max0} is the initial friction coefficient at high velocity, while Δf and γ are pressure parameters that require experimental calibration. The parameter p represents the instantaneous bearing pressure. This relationship is further supported by the previous discussion, where the parameter α varies with changes in pressure. Additionally, Dao et al. [33] proposed equations for f_{min} and f_{max} as functions of the axial load on an FPB. These equations, given in Equations (3) and (4), respectively, express f_{min} and f_{max} in terms of the axial load W (in Newtons).

$$f_{min} = 8.701W^{-0.34} \tag{3}$$

$$f_{max} = 17.239W^{-0.38} \tag{4}$$

3. Analytical Model and Methodology

3.1. Bridge Structural Modelling

The study involves five distinct hypothetical multi-span continuous box-girder RC bridges designed by the researchers to represent a specific type of bridge in California [35,36]. The assumed modulus of elasticity of the concrete for the bridges is 27,790 MPa. All bridges share uniform characteristics, including span lengths, pier type, and structural element dimensions, with the sole exception being the deck depth. Figure 3 provides longitudinal and transverse elevation views of the bridges, along with structural element dimensions. Notably, Y_{CM} in Figure 3 denotes the center of mass of the deck.

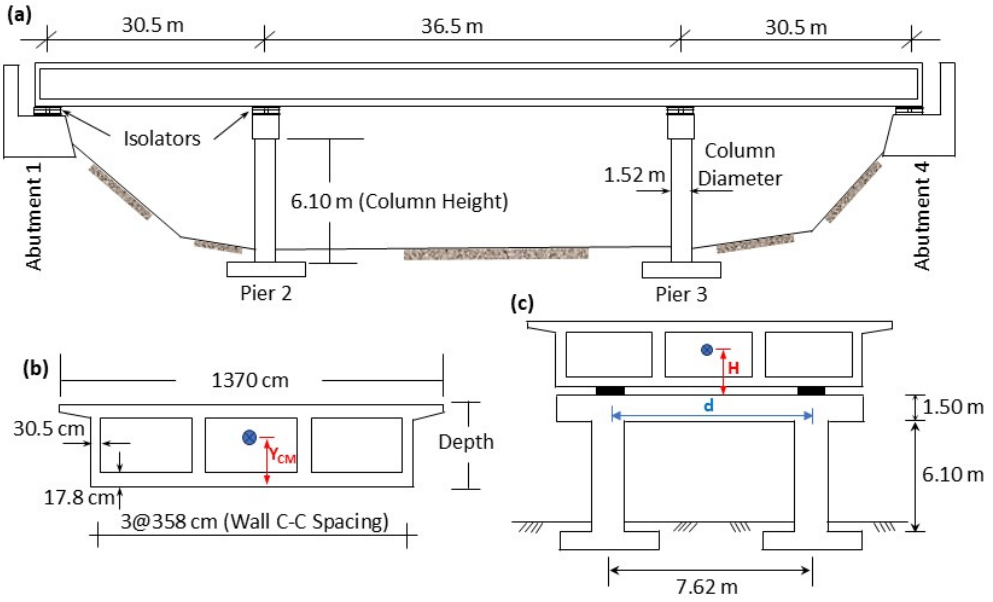


Figure 3. Schematic view of the bridges (**a**) longitudinal elevation, (**b**) deck cross section, (**c**) transverse elevation.

The five bridges are differentiated solely by their deck depth, which allows for the utilization of different aspect ratios (ARs) and, consequently, mass ratios. The AR of a deck is defined as the ratio between the relative distance (d) of two FPBs and the vertical distance (H) from the center of mass of the deck to the base of the FPBs, as illustrated in Figure 3. The AR estimation is provided in Equation (5). In this study, the mass ratio is defined as the ratio between the mass of the substructure (pier) and the tributary mass of the superstructure (deck) supported by the corresponding pier. The chosen deck depths and the necessary bridge parameters for estimating ARs of 4, 5, 6, 7, and 9 are provided in Table 1, along with the corresponding mass ratios. The bridges are labeled in Table 1 as

B-AR#, where # indicates the aspect ratio of the corresponding bridge. The height of the considered FPBs is 22.9 cm, and their details are elaborated upon in the subsequent section.

$$AR = \frac{d}{H} \tag{5}$$

Table 1. Required bridge parameters to estimate AR and mass ratio.

Bridge	Deck Depth (cm)	Y_{CM} (cm)	H (cm)	d (cm)	AR	m_{sub} (kNs^2/m)	m_{super} (kNs^2/m)	Mass Ratio
B-AR4	300	164	187	762	4	82.7	651.2	0.13
B-AR5	245	130	153	762	5	82.7	594	0.14
B-AR6	195	104	127	762	6	82.7	542	0.15
B-AR7	160	85.7	108.7	762	7	82.7	505.4	0.16
B-AR9	115	61.79	84.79	762	9	82.7	458.6	0.18

The OpenSees (v3.5.0) [17] analysis program was employed for modeling the bridges, incorporating the spine model approach as proposed by Ryan and Mojidra [36], Aviram et al. [37], and Mackie et al. [38]. The bridge superstructure is assumed to remain elastic and is designed as a capacity-protected system [39]. Furthermore, isolators are strategically implemented with the primary objective of concentrating nonlinearity within them, preventing the piers from exceeding the elastic limit. Consequently, the bridge superstructure, cap beam, and columns were modeled in OpenSees (v3.5.0) [17] using the *elasticBeamColumn* element. The columns were fixed at their base, and the isolators on the abutments were also fixed, assuming the abutments to be perfect restraints. Due to the placement of the elastic beam-column elements at the center of gravity of the structural members, rigid connections were used to connect the column-cap beam, cap beam-isolator, and isolator-deck. Each superstructure span is divided into 10 segments, with translational and rotational masses of tributary length assigned to each node. Rotational inertia about the longitudinal, transverse, and vertical axes is estimated using Equations (6)–(8), where m, L_{trib}, and d_w represent mass, tributary length, and deck width, respectively. Figure 4 provides a visual representation of the general bridge modeling approach in OpenSees (v3.5.0) [17]. The participation of soil and abutment mass, as well as soil–structure interaction, was omitted from the bridge modeling since the primary objective is to evaluate the influence of the friction coefficient assumption in FPBs on the overall response of the considered bridge type.

$$I_{long} = \frac{mL_{trib}d_w^2}{12} \tag{6}$$

$$I_{trans} = \frac{mL_{trib}^3}{12} \tag{7}$$

$$I_{vertical} = \frac{mL_{trib}\left(L_{trib}^2 + d_w^2\right)}{12} \tag{8}$$

The OpenSees (v3.5.0) [17] model was validated by comparing its modal properties with the results obtained from the analysis of Bridge B-AR7 in the CSI Bridge (v18.2.0) [40] software program under non-isolated conditions. Moreover, fundamental section properties of the structural members, including the superstructure, to be assigned to the OpenSees (v3.5.0) [17] models were derived from the analytical models in CSI Bridge (v18.2.0) [40]. The columns and cap beams were defined with elastic frame elements, while shell elements were used to model the superstructure. A general view of the CSI Bridge (v18.2.0) [40]

model is shown in Figure 5. Table 2 presents the longitudinal, transverse, and vertical mode periods of Bridge B-AR7, estimated using both OpenSees (v3.5.0) [17] and CSI Bridge (v18.2.0) [40]. The comparison reveals that the OpenSees (v3.5.0) [17] modeling approach satisfactorily represents the higher-fidelity CSI Bridge (v18.2.0) [40] model, as shown by the results in Table 2.

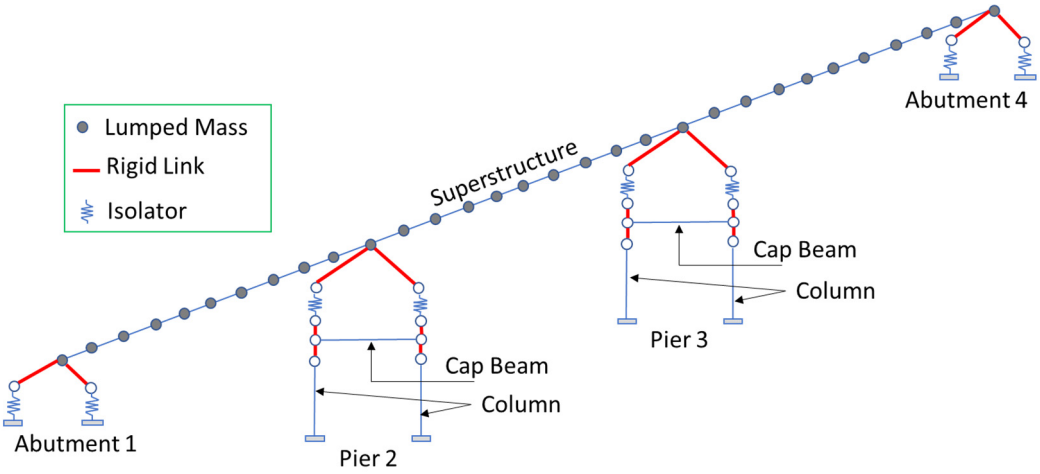


Figure 4. A general representation of bridge modelling in OpenSees (v3.5.0) [17].

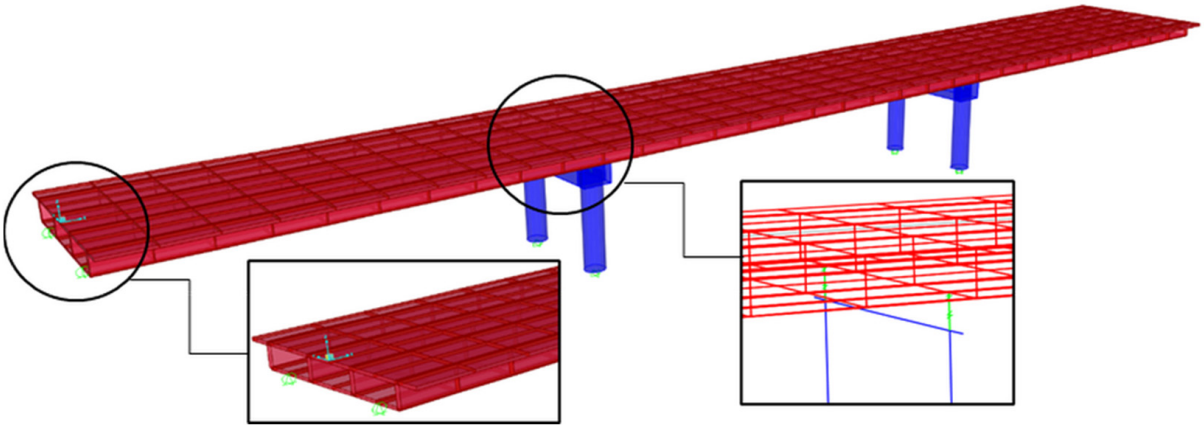


Figure 5. A general view of the CSI Bridge (v18.2.0) [40] model of Bridge B-AR7.

Table 2. Fundamental periods of Bridge B-AR7 obtained from both OpenSees (v3.5.0) [17] and CSI Bridge (v18.2.0) [40].

Direction	OpenSees	CSI Bridge
Longitudinal	0.770 s.	0.765 s.
Transverse	0.353 s.	0.387 s.
Vertical	0.190 s.	0.208 s.

3.2. Isolators and Friction Modeling

In this study, a DPB was used as the isolator on bridges. The cross-section drawing of the isolator is represented in Figure 6, while its design parameters are given in Table 3.

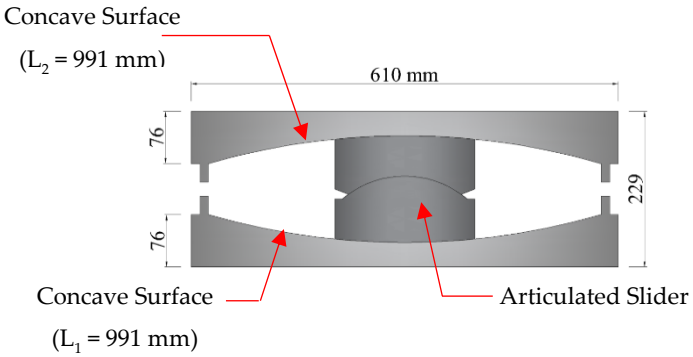


Figure 6. Cross-section view of the considered DPB.

Table 3. Design parameters of the considered DPB.

Parameters	Value
Target friction ($\mu_1 = \mu_2$)	0.08
Effective pendulum length L (mm)	1882
Pendulum period T (s)	2.75

Although various materials can be used in FPBs, the concave surface and articulated slider are typically made of stainless steel, while the concave plates are made of ductile steel. A common practice is to coat articulated sliders with PTFE or PTFE-composite materials, creating a PTFE-on-steel interface for enhanced durability and reduced friction [6,22,30]. Different types of PTFE are available on the market, including filled-PTFE, unfilled-PTFE, and woven-PTFE. However, the specific type of PTFE coating was not specified in this study, as the considered wide range of α is expected to adequately represent the potential variations.

Isolators were modeled in OpenSees (v3.5.0) [17] using the *SingleFPBearing* element, with various parameters considered, including initial stiffness, vertical stiffness, effective length of the pendulum (L), friction model, and friction coefficient (μ). The initial stiffness was determined based on a 0.25 mm yield displacement assumption [29], while the vertical stiffness was estimated for a vertical period of 0.03 s., considering the average weight applied to the isolators.

As previously discussed, this study examines the influence of contact pressure, different friction models, and their variable characteristics on box-girder bridges, with a particular focus on deck aspect ratio and mass ratio. The three primary friction models analyzed, available in the OpenSees (v3.5.0) [17] library, include the Coulomb, velocity-dependent, and velocity-pressure-dependent friction models. The Coulomb friction model incorporates only the friction coefficient, which was set to 0.08 as indicated in Table 3.

The parameters required to define the velocity-dependent friction model are f_{min}, f_{max}, and α. Values for f_{min} and f_{max} were estimated using Equations (3) and (4), based on the approach suggested by Dao et al. [33]. Since the coefficients in Equations (3) and (4) were derived for an FBP with a design friction coefficient of 0.08, this value was selected for the friction coefficient in this study to ensure consistency. The axial load W was calculated as the tributary weight on each pier and abutment. The parameter α was varied with values of 20, 30, 54.41, 83.4, 100, and 200 to cover a broad range suggested in the literature, as explained in Section 2, excluding the Teflon layer material properties and pressure rate. This approach allows for an investigation into the significance of selecting an accurate α value, as well as the relationship between pressure and aspect ratio. Moreover, the main purpose of selecting this broad range of α, regardless of material and pressure, is to demonstrate how the selected α value might affect the overall behavior of the isolator and the bridge.

The final friction model considered is the velocity-pressure-dependent model, as given in Equation (2), to evaluate the influence of bearing pressure on the friction coefficient and, consequently, the seismic behavior of box-girder bridges. f_{max0} in Equation (2) was calculated using Equation (4), while Δf and γ were assumed to be 0.07 and 0.012 MPa^{-1}, respectively, as suggested by Constantinou et al. [29].

3.3. Ground Motion Records and Time History Analysis

Nonlinear time history analyses were conducted in OpenSees (v3.5.0) [17], and the equations of motion were solved using the Newmark-β Method, which is one of the direct integration methods. The γ and β constants of the Newmark-β Method were set to 0.5 and 0.25, respectively, with the average acceleration assumption, which is unconditionally stable.

Nonlinear time history analyses (NLTHAs) were performed for 11 ground motion (GM) records selected from the PEER NGA [41] database, each with two horizontal components. The shear wave velocity of the selected GMs ranges from 760 m/s to 1520 m/s, corresponding to site class B, and the magnitudes are greater than 6. The GMs were scaled to a target spectrum to meet code-compliant intensity using the procedure defined in ASCE 7-22 [24]. Although ASCE 7-22 [24] was developed for buildings, it provides general guidance for GM selection and scaling procedures. While ASCE 7-22 [24] offers two scaling methods: amplitude scaling and spectral matching, amplitude scaling was chosen in this study to preserve the frequency content of the GMs. The GMs were scaled to match the 5%-damped target spectrum using a least-squares approach over the period range of 0.30 to 2.50 s covering the modes of the isolated structure. In accordance with ASCE 7-22 [24], scaling was based on the maximum direction spectrum (ROTD100). Two components of each GMs were rotated by an angle θ from 0° to 180° in 10° increments. The 5%-damped response spectrum was estimated for each rotated acceleration time history (a_θ (t)) and the maximum spectral acceleration across all rotation angles defined the ROTD100 spectrum. Each ROTD100 spectrum was then scaled to match the target spectrum. After initial scaling, slight adjustments were made to ensure that the average maximum direction spectrum of the ground motion suite remained above 90% of the target over the scaling range. The scaling factors range from 0.33 to 3, and each was applied to the acceleration time history of its corresponding GM. Figure 7 shows the maximum direction spectrum of the GMs, along with their average and the 5% target spectrum, whereas list of the GMs with their related characteristics is given in Table 4. Moreover, the time step of each GM was set to 0.005 s. to increase the reliability of the direct integration solution.

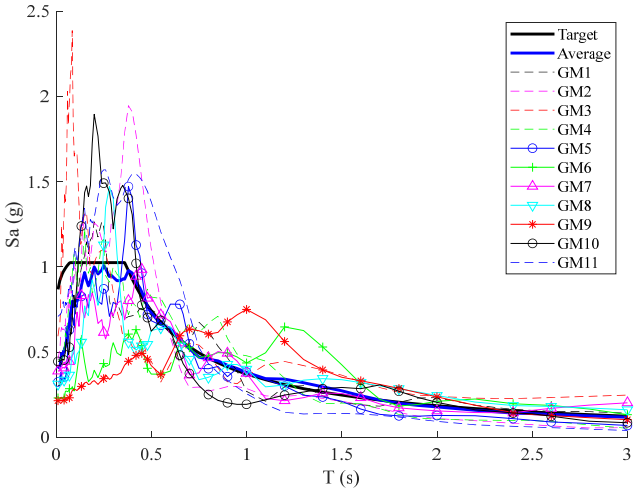


Figure 7. Maximum direction spectrums of the selected GMs along with their average and 5% target spectrum.

Table 4. Ground motion suite characteristics.

Tag	Earthquake	Year	Station Name	Mag	R_{jb} (km)	Scale Factor	Scaled PGA (g)
GM1	Tabas, Iran	1978	Tabas	7.35	1.79	0.345	0.303
GM2	Loma Prieta, CA	1989	Gilroy Array #1	6.93	8.84	0.915	0.456
GM3	Landers, CA	1992	Lucerne	7.28	2.19	0.738	0.593
GM4	Northridge-01, CA	1994	LA-Wonderland Ave	6.69	15.11	2.759	0.459
GM5	Northridge-01, CA	1994	Vasquez Rocks Park	6.69	23.1	1.882	0.325
GM6	Kobe, Japan	1995	Kobe University	6.9	0.9	0.700	0.231
GM7	Kocaeli, Turkey	1999	Gebze	7.51	7.57	1.424	0.389
GM8	Kocaeli, Turkey	1999	Izmit	7.51	3.62	1.260	0.312
GM9	Loma Prieta, CA	1989	Los Gatos-Lexington Dam	6.93	3.22	0.464	0.215
GM10	Tottori, Japan	2000	SMNH10	6.61	15.58	1.845	0.445
GM11	Parkfield-02, CA	2004	Parkfield-Turkey Flat #1 0 M	6	4.66	2.765	0.709

4. Results and Discussion

4.1. The Aspect Ratio

To assess the influence of deck aspect ratio and the considered friction models on the seismic response of box-girder RC bridges, isolator displacement (U_{iso}), defined as the peak displacement in any isolator over the motion history, along with isolator shear force (T_{iso}) and pier shear force (T_{pier}), representing the peak sum of these forces across all individual isolators or bridge piers over time, were compared. Both isolator and pier shear forces were normalized by the superstructure (deck) weight (W_s) and the total bridge weight (W_b) carried by the piers (excluding the portion supported by abutments), respectively, to provide insight into the magnitude of the estimated forces. Analysis results for various friction models are presented in Figure 8, showing the average peak responses of bridges subjected to 11 ground motion records. Additionally, C, V, and VP represent the Coulomb friction model, the velocity-dependent friction model, and the velocity-pressure-dependent friction model, respectively, while the parameter α denotes the experimentally determined transition rate.

Figure 8a,b show that both the Coulomb and velocity-dependent friction models result in similar isolator displacements in both directions, with the Coulomb model producing slightly smaller displacements. In contrast, the velocity-pressure-dependent friction model leads to a significant increase in isolator displacement compared to the other two models.

The Coulomb friction model results in isolator displacements of approximately 72 mm in the transverse direction and 60 mm in the longitudinal direction, regardless of AR. With the velocity-dependent friction model, transverse isolator displacement decreases as AR increases, from 88 mm for AR4 to 78 mm for AR9. Notably, α has little effect on isolator displacement in this model. In contrast, in the velocity-pressure-dependent friction model, AR has minimal impact on isolator displacement, while increasing α leads to larger displacements. For this model, transverse displacement increases from 180 mm at α = 20 to 192 mm at α = 200, while longitudinal displacement increases from 161 mm to 175 mm over the same range.



Figure 8. Peak responses of bridges due to various friction models.

Regarding the isolator shear coefficient (T_{iso}/W_s), all friction models yield similar results, regardless of AR and α. The Coulomb model produces an isolator shear coefficient of approximately 12% in the transverse direction and 10% in the longitudinal direction across all AR values. The velocity-dependent friction model results in a shear coefficient of 10% in the transverse direction and 9% in the longitudinal direction, remaining consistent across all AR and α values. For the velocity-pressure-dependent model, increasing α causes a slight, negligible increase in the isolator shear coefficient, independent of AR. Specifically, in the transverse direction, the coefficient is 12% for α = 20 and decreases slightly to 10% for α = 200. In the longitudinal direction, it is 10% for α = 20 and decreases to 9% for α = 200.

The pier shear coefficient (T_{pier}/W_b) is slightly affected by the friction models. The parameters α and AR have no significant impact on the estimated pier shear coefficient, except for α = 20 in the velocity-pressure-dependent model, where the coefficient is approximately 1% higher than for other α values. In both directions, the Coulomb model produces a pier shear coefficient ranging from 9% to 10% as AR increases from 4 to 9. The velocity-dependent model yields coefficients between 7.5% and 9% over the same AR range, irrespective of α. The velocity-pressure-dependent model results in pier shear coefficients between 8% and 9% for all α values, except for α = 20 in the transverse direction, where it reaches 9.5%.

To further illustrate the impact of these friction models relative to the Coulomb model, Figure 9 presents the ratio of peak responses from the velocity-dependent and velocity-pressure-dependent models to those from the Coulomb model for varying AR and α. The velocity-dependent friction model increases isolator displacement compared to the Coulomb model, with displacement ratios ranging from 1.20 to 1.09 for AR values of 4 to 9 in the transverse direction and from 1.15 to 1.06 in the longitudinal direction, regardless of α. In contrast, the isolator displacement ratio for the velocity-pressure-dependent model remains nearly constant across AR values but increases with α. Specifically, isolator displacement in this model is 2.50 to 2.66 times greater than in the Coulomb model for

α values of 20 to 200 in the transverse direction, and 2.78 to 3.00 times greater in the longitudinal direction.

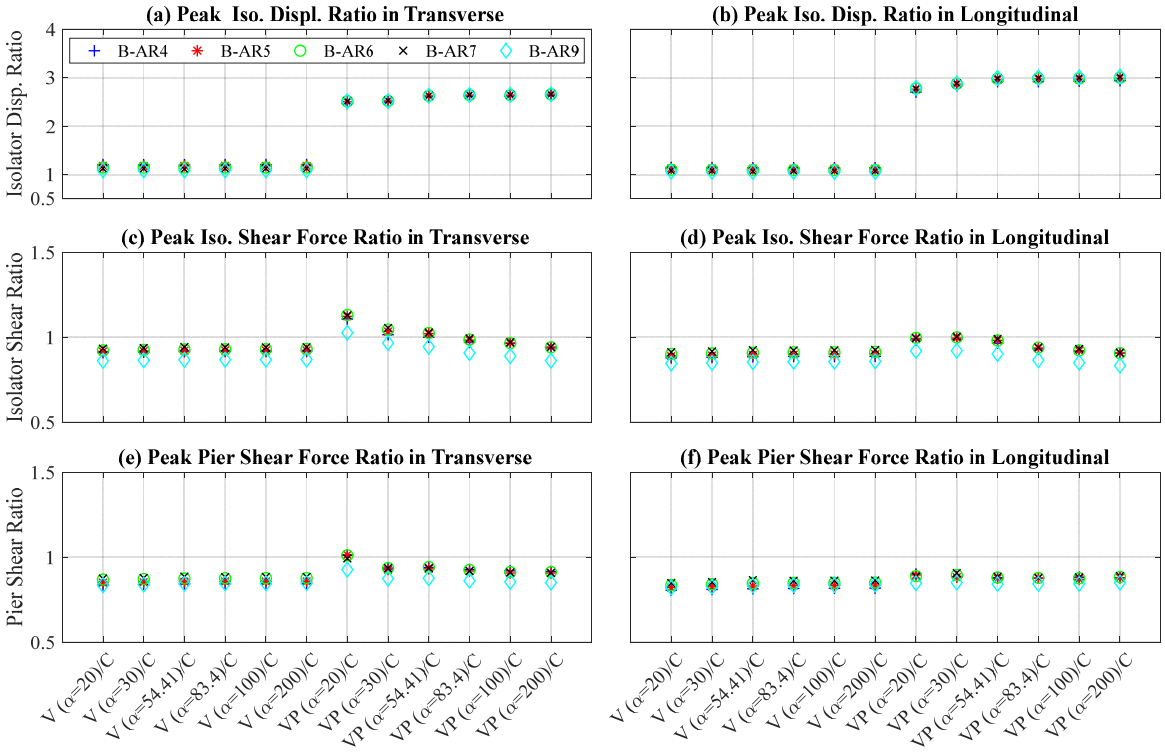


Figure 9. The ratio of peak responses for bridges obtained for the velocity- and velocity-pressure-dependent friction models to those obtained for the Coulomb friction model.

When using the velocity-dependent friction model, the isolator shear force ratio decreases by approximately 8% compared to the Coulomb friction model in the transverse direction for all AR values, except when AR = 9, regardless of α. For AR = 9, this reduction increases to nearly 14% across all α values. In the longitudinal direction, the velocity-dependent friction model results in an approximately 11% reduction in isolator shear force for AR values ranging from 4 to 7, regardless of α, and a 15% reduction when AR = 9. For the velocity-pressure-dependent friction model, the isolator shear force ratio decreases as α increases. When α = 20, this model predicts a 12% increase in transverse isolator shear force compared to the Coulomb model for AR values from 4 to 7, while for AR = 9, the increase is only 3%. When α = 30 or 54.41, the results from the velocity-pressure-dependent model closely match those from the Coulomb model. However, for α = 83.4, 100, and 200, the velocity-pressure-dependent model predicts smaller transverse isolator shear forces, with reductions averaging 5% for AR values from 4 to 7. For AR = 9, the transverse isolator shear force decreases by 3% to 14% as α ranges from 30 to 200. In the longitudinal direction, the velocity-pressure-dependent model consistently predicts lower isolator shear forces than the Coulomb model, with reductions ranging from 2% to 10% for α values between 20 and 200 and AR values from 4 to 7. For AR = 9, this reduction increases to between 8% and 17% as α varies from 20 to 200.

Overall, the velocity-dependent friction model results in smaller pier shear forces compared to the Coulomb friction model. The reduction in pier shear force due to this model ranges from 12% to 16% in the transverse direction and 14% to 20% in the longitudinal direction across all AR values. Additionally, variations in α have little to no effect on the velocity-dependent model's influence on pier shear force. The velocity-pressure-dependent friction model also reduces pier shear forces compared to the Coulomb model, but its effect varies with α in the transverse direction while remaining unaffected by α in the

longitudinal direction. Similar to the velocity-dependent model, AR does not significantly impact the pier shear force reduction caused by the velocity-pressure-dependent model. In the transverse direction, the pier shear force reduction relative to the Coulomb model decreases from 10% to 1% as α increases for AR values from 4 to 7. However, for AR = 9, the reduction increases from 7% to 15% with α. In the longitudinal direction, the pier shear force reduction remains nearly constant at 11% for AR values from 4 to 7 and increases to 15% for AR = 9.

4.2. The Mass Ratio

In this study, another key parameter that varies among bridges is the mass ratio—the ratio of substructure mass to superstructure mass. This variation is achieved by adjusting the deck cross-section height, thereby altering the superstructure mass while keeping the substructure mass constant. As noted by Koval et al. [42] and Rasouli et al. [43], the mass ratio may influence bridge responses independently of AR. To investigate this effect, the mass ratio of Bridge B-AR6 was hypothetically modified to 0.12, 0.15, and 0.21 by adjusting only the substructure mass while maintaining a constant AR. Figure 10 presents the peak responses of the bridges for different mass ratios.



Figure 10. Peak responses for bridges due to various ratios of substructure mass to superstructure mass for B-AR6.

Figure 10a,b show trends similar to those observed in Figure 8. The peak isolator displacement in the transverse direction is approximately 70 mm and 80 mm for the Coulomb and velocity-dependent friction models, respectively, regardless of the mass ratio. In the longitudinal direction, the peak isolator displacement remains around 62 mm for both models. For the velocity-pressure-dependent friction model, the peak isolator displacement in the transverse direction increases slightly with α, independent of the mass ratio, ranging from 180 mm to 192 mm as α changes from 20 to 200. In the longitudinal direction, this displacement varies between 160 mm and 176 mm for the same range of α.

According to Figure 10c,d, the mass ratio has a negligible effect on the isolator shear coefficient. The Coulomb friction model results in an isolator shear coefficient of approx-

imately 11% in the transverse direction and 10% in the longitudinal direction. For the velocity-dependent friction model, the coefficient remains around 10% in both directions, regardless of α. In contrast, the velocity-pressure-dependent friction model shows a decreasing trend in the isolator shear coefficient with increasing α, dropping from 12.5% to 9% in the transverse direction and from 10% to 9% in the longitudinal direction.

The pier shear coefficient increases slightly with a higher mass ratio, with the effect being more pronounced in the longitudinal direction, particularly for the velocity-pressure-dependent friction model. For the Coulomb friction model, the pier shear coefficient is 9.4% in both directions for mass ratios of 0.12 and 0.15, increasing to 11% for a mass ratio of 0.21. Similarly, the velocity-dependent friction model results in a pier shear coefficient of approximately 8.3% for mass ratios of 0.12 and 0.15, rising to about 9.4% for a mass ratio of 0.21.

In the transverse direction, the pier shear coefficient for the velocity-pressure-dependent friction model decreases as α increases from 20 to 200. For mass ratios of 0.12 and 0.15, it declines from 9.6% to 8.5%, while for a mass ratio of 0.21, it remains steady at approximately 10%, regardless of α. In the longitudinal direction, the pier shear coefficient remains at 8.1%, 8.7%, and 11% for mass ratios of 0.12, 0.15, and 0.21, respectively, independent of α.

Figure 11 illustrates the ratio of peak bridge responses for a mass ratio of 0.21 to those for a mass ratio of 0.12, providing insight into the effect of mass ratio on these responses. As shown in Figure 11a, the mass ratio has no significant impact on isolator displacement in either direction for the friction models considered, except for the Coulomb and velocity-dependent friction models in the longitudinal direction. Figure 11b demonstrates that the mass ratio has a negligible effect on the isolator shear force across all cases.

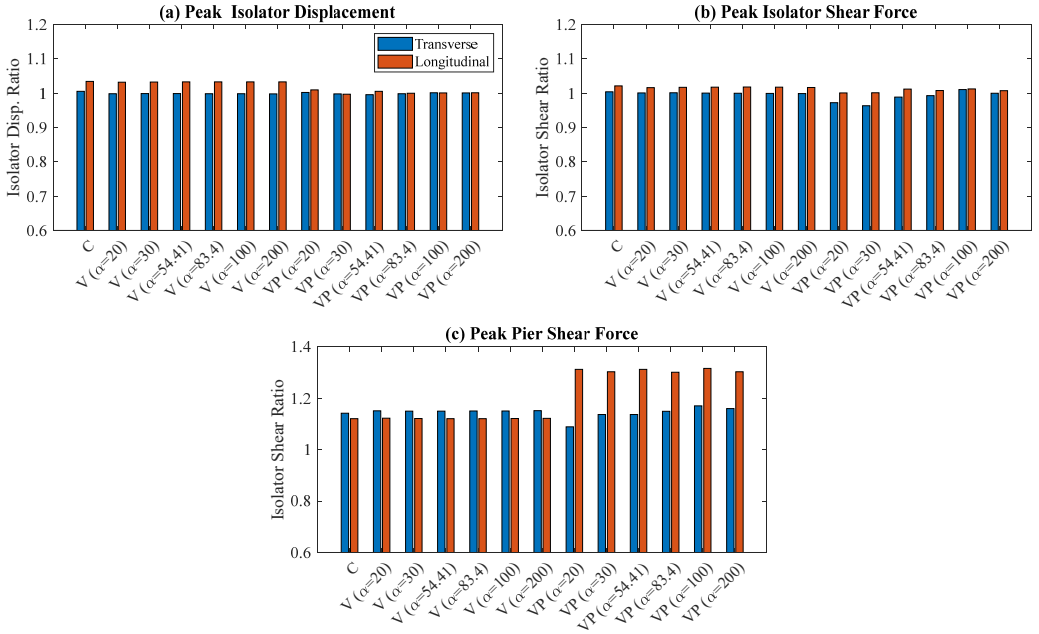


Figure 11. The ratio of the peak bridge responses obtained for a mass ratio of 0.21 to those obtained for a mass ratio of 0.12 ($m_R = 0.21/m_R = 0.12$).

In contrast, Figure 11c reveals that the mass ratio substantially influences the pier shear force, regardless of the parameter α. Specifically, increasing the mass ratio to 0.21 results in an approximately 15% increase in pier shear force in the transverse direction for all friction models compared to a mass ratio of 0.12. In the longitudinal direction, the Coulomb and velocity-dependent friction models lead to a 12% increase in pier shear force, whereas the

velocity-pressure-dependent friction model produces a more pronounced 30% increase, irrespective of α.

5. Conclusions

This study aimed to evaluate the impact of different friction models used to simulate friction pendulum bearings on the seismic response of box-girder RC bridges. Additionally, it investigated the influence of deck aspect ratio and the mass ratio between the substructure and superstructure on the effects of these friction models. To achieve this, five three-span box-girder RC bridges with double pendulum bearings were analyzed. The bridges varied in deck height, which determined their aspect ratios, while other parameters remained constant. Their mass ratios differed because the substructure mass was fixed while the superstructure mass increased with deck height. The analytical models incorporated Coulomb, velocity-dependent, and velocity-pressure-dependent friction models. Nonlinear time history analyses were conducted using 11 pairs of ground motion records to evaluate peak seismic responses, including isolator displacement, isolator shear force, and pier shear force. The findings of this study led to the following conclusions:

- The velocity-pressure-dependent friction model results in isolator displacements that are nearly 2.5 to 3 times larger in both directions compared to those produced by the Coulomb and velocity-dependent friction models, regardless of the aspect ratio or rate parameter α. This result indicates that the contact pressure effect should be considered in friction modeling during the design phase to estimate a more conservative isolator displacement capacity.
- The velocity-dependent friction model results in a decrease in the isolator shear force for all α and AR values compared to the Coulomb model, although the decrease is negligible. The most pronounced reduction was observed for an AR of 9, with a decrease of nearly 14%.
- The effect of the velocity-pressure-dependent friction model on the isolator shear force varies with direction and the parameter α, as an increase in α results in a decrease in isolator shear force. This model leads to a 12% increase in isolator shear force in the transverse direction compared to the Coulomb friction model when α = 20 and AR ranges from 4 to 7. However, the increase is negligible for an AR of 9. When α exceeds 83.4, the velocity-pressure-dependent model predicts smaller transverse isolator shear forces than the Coulomb model. In the longitudinal direction, the velocity-pressure-dependent friction model consistently results in a reduction in isolator shear force compared to the Coulomb friction model.
- Both the velocity-dependent and velocity-pressure-dependent friction models result in smaller pier shear forces in both directions compared to the Coulomb model, regardless of the rate parameter α and the AR. However, when α is 20 in the velocity-pressure-dependent friction model, the results are closer to those of the Coulomb friction model.
- In general, the mass ratio does not influence the effects of friction models on the peak responses. Specifically, the mass ratio has no impact on isolator displacement or shear forces, but it affects the pier shear, particularly for the velocity-pressure-dependent friction model in the longitudinal direction.
- According to the results, the differences in responses depend more on the mass ratio than on the deck aspect ratio.
- The results showed that the suggested values of the rate parameter α for different PTFE composite materials used in modeling an FPB have insignificant effects on the seismic responses of box-girder RC bridges, particularly for the velocity-dependent friction model and any α value can be selected for this model. However, α should

be carefully chosen for the velocity-pressure-dependent friction model, as $\alpha = 20$ produces different results compared to other α values.

- The results of this study reveal that the velocity-pressure-dependent friction model should be considered in the analytical model of FPBs to estimate more consistent responses.

These results provide valuable insights for optimizing bridge designs and selecting appropriate friction models and parameters to enhance seismic performance. Future research could explore extending the study to include various bridge configurations, soil-structure interaction, and the vertical component of ground motions.

Funding: This research received no external funding.

Data Availability Statement: The datasets generated and/or analyzed during the current study are available from the corresponding author upon reasonable request.

Conflicts of Interest: The author has no relevant financial or non-financial interests to disclose.

References

1. Ryan, K.L.; Chopra, A.K. Estimating the seismic displacement of friction pendulum isolators based on non-linear response history analysis. *Earthq. Eng. Struct. Dyn.* **2004**, *33*, 359–373. [CrossRef]
2. Buckle, I.G.; Constantinou, M.C.; Dicleli, M.; Ghasemi, H. *Seismic Isolation of Highway Bridges*; MCEER-06-SP07; State University of New York at Buffalo: Buffalo, NY, USA, 2006.
3. Morgan, T.A.; Mahin, S.A. Achieving reliable seismic performance enhancement using multi-stage friction pendulum isolators. *Earthq. Eng. Struct. Dyn.* **2010**, *39*, 1443–1461. [CrossRef]
4. Wen, J.; Han, Q.; Du, X. Shaking table tests of bridge model with friction sliding bearings under bi-directional earthquake excitations. *Struct. Infrastruct. Eng.* **2019**, *15*, 1264–1278. [CrossRef]
5. Shang, J.; Tan, P.; Zhang, Y.; Han, J.; Qin, J. Experimental and analytical investigation of variable friction pendulum isolator. *Eng. Struct.* **2021**, *243*, 112575. [CrossRef]
6. Calvi, P.M.; Calvi, G.M. Historical development of friction-based seismic isolation systems. *Soil Dyn. Earthq. Eng.* **2018**, *106*, 14–30. [CrossRef]
7. Constantinou, M.C.; Whittaker, A.S.; Kalpakidis, Y.; Fenz, D.M.; Warn, G.P. *Performance of Seismic Isolation Hardware Under Service and Seismic Loading*; MCEER-07-12; State University of New York at Buffalo: Buffalo, NY, USA, 2007.
8. Constantinou, M.C.; Mokha, A.; Reinhorn, A.M. *Experimental and Analytical Study of a Combined Sliding Disc Bearing and Helical Steel Spring Isolation System*; NCEER-90-0019; State University of New York at Buffalo: Buffalo, NY, USA, 1990.
9. Mokha, A.; Constantinou, M.C.; Reinhorn, A.M. Teflon bearings in base isolation I: Testing. *J. Struct. Eng.* **1990**, *116*, 438–454. [CrossRef]
10. Dolce, M.; Cardone, D.; Croatto, F. Frictional behavior of steel-PTFE interfaces for seismic isolation. *Bull. Earthq. Eng.* **2005**, *3*, 75–99. [CrossRef]
11. Quaglini, V.; Dubini, P.; Poggi, C. Experimental assessment of sliding materials for seismic isolation systems. *Bull. Earthq. Eng.* **2012**, *10*, 717–740. [CrossRef]
12. Kumar, M.; Whittaker, A.S.; Constantinou, M.C. Characterizing friction in sliding isolation bearings. *Earthq. Eng. Struct. Dyn.* **2015**, *44*, 1409–1425. [CrossRef]
13. Peng, P.; Dongbin, Z.; Yi, Z.; Yachun, T.; Xin, N. Development of a tunable friction pendulum system for semi-active control of building structures under earthquake ground motions. *Earthq. Eng. Struct. Dyn.* **2018**, *47*, 1706–1721. [CrossRef]
14. Xu, Y.; Guo, T.; Yan, P. Design optimization of triple friction pendulums for base-isolated high-rise buildings. *Adv. Struct. Eng.* **2019**, *22*, 2727–2740. [CrossRef]
15. Solgi, M.; Rajabi, E.; Amiri, G.G.; Dehkordi, M.R. Seismic resilience evaluation of a 3D steel moment frame building with triple friction pendulum isolators. *Structures* **2025**, *72*, 108075. [CrossRef]
16. *SAP2000; Structural Analysis and Design*; Computers and Structures Inc.: Walnut Creek, CA, USA, 2025. Available online: https://www.csiamerica.com/products/sap2000 (accessed on 16 January 2025).
17. OpenSees; Open Systen for Earthquake Engineering Simulation. Available online: https://opensees.berkeley.edu (accessed on 20 May 2023).
18. Fenz, D.M.; Constantinou, M.C. Modeling triple friction pendulum bearings for response-history analysis. *Earthq. Spectra* **2008**, *24*, 1011–1028. [CrossRef]
19. Cardone, D.; Gesualdi, G.; Brancato, P. Restoring capability of friction pendulum seismic isolation systems. *Bull. Earthq. Eng.* **2015**, *13*, 2449–2480. [CrossRef]

20. Ponzo, F.C.; Di Cesare, A.; Leccese, G.; Nigro, D. Shake table testing on restoring capability of double concave friction pendulum seismic isolation systems. *Earthq. Eng. Struct. Dyn.* **2017**, *46*, 2337–2353. [CrossRef]
21. Özşahin, E.; Pekcan, G.; Borekci, M. Design of shear keys for mitigating seismic response due to translational and torsional ground motions. *Eng. Struct.* **2024**, *312*, 118195. [CrossRef]
22. Lomiento, G.; Bonessio, N.; Benzoni, G. Friction model for sliding bearings under seismic excitation. *J. Earthq. Eng.* **2013**, *17*, 1162–1191. [CrossRef]
23. Calvi, G.M.; Ceresa, P.; Casarotti, C.; Bolognini, D.; Auricchio, F. Effects of axial force variation in the seismic response of bridges isolated with friction pendulum systems. *J. Earthq. Eng.* **2004**, *8*, 187–224. [CrossRef]
24. *ASCE/SEI 7-22*; Minimum Design Loads for Buildings and Other Structures. American Society of Civil Engineers: Reston, VA, USA, 2022.
25. *AASHTO*, 4th ed.; Guide Specifications for Seismic Isolation Design; American Association of State Highway and Transportation Officials: Washington, DC, USA, 2014.
26. *EN 15129*; Anti-Seismic Devices. European Standard: Brussels, Belgium, 2018.
27. Mokha, A.; Constantinou, M.C.; Reinhorn, A.M. *Teflon Bearings in Aseismic Base Isolation: Experimental Studies and Mathematical Modeling*; NCEER-88/0038; State University of New York at Buffalo: Buffalo, NY, USA, 1988.
28. Campbell, T.I.; Pucchio, J.B.; Roeder, C.W.; Stanton, J.F. Frictional Characteristics of PTFE Used in Slide Surfaces of Bridge Bearings. In Proceedings of the 3rd World Congress on Joint Sealing and Bearing Systems for Concrete Structures, Toronto, ON, Canada, 27–31 October 1991; pp. 847–870.
29. Constantinou, M.C.; Tsopelas, P.; Kim, Y.S.; Okamoto, S. *NCEER-Taisei Corporation Research Program on Sliding Seismic Isolation Systems for Bridges: Experimental and Analytical Study of a Friction Pendulum System (FPS)*; NCEER-93-0020; State University of New York at Buffalo: Buffalo, NY, USA, 1993.
30. Tsopelas, P.; Constantinou, M.C.; Kim, Y.S.; Okamoto, S. Experimental study of FPS system in bridge seismic isolation. *Earthq. Eng. Struct. Dyn.* **1996**, *25*, 65–78. [CrossRef]
31. Mokha, A.S.; Constantinou, M.C.; Reinhorn, A.M. Verification of friction model of Teflon bearings under triaxial load. *J. Struct. Eng.* **1993**, *119*, 240–261. [CrossRef]
32. Constantinou, M.C.; Tsopelas, P.; Kasalanati, A.; Wolff, E.D. *Property Modification Factors for Seismic Isolation Bearings*; MCEER-99-0012; State University of New York at Buffalo: Buffalo, NY, USA, 1999.
33. Dao, N.D.; Ryan, K.L.; Sato, E.; Sasaki, T. Predicting the displacement of triple pendulum™ bearings in a full-scale shaking experiment using a three-dimensional element. *Earthq. Eng. Struct. Dyn.* **2013**, *42*, 1677–1695. [CrossRef]
34. Hwang, J.S.; Chang, K.C.; Lee, G.C. Quasi-static and dynamic sliding characteristics of Teflon-Stainless steel interfaces. *J. Struct. Eng.* **1990**, *116*, 2747–2762. [CrossRef]
35. Ramanathan, K. Next Generation Seismic Fragility Curves for California Bridges Incorporating the Evolution in Seismic Design Philosophy. Ph.D. Dissertation, Georgia Institute of Technology, Atlanta, GA, USA, 2012.
36. Ryan, K.L.; Mojidra, R. Analysis of effect of vertical ground shaking in bridges isolated with spherical sliding bearings. *Earthq. Eng. Struct. Dyn.* **2023**, *52*, 5010–5032. [CrossRef]
37. Aviram, A.; Mackie, K.R.; Stojadinovic, B. Effect of abutment modeling on the seismic response of bridge structures. *Earthq. Eng. Eng. Vib.* **2008**, *7*, 395–402. [CrossRef]
38. Mackie, K.R.; Scott, M.H.; Johnson, K.; Al-Ramahee, M.; Steijlen, M. *Nonlinear Time History Analysis of Ordinary Standard Bridges*; No. CA17-2755; California Department of Transportation, Division of Engineering Services: Sacramento, CA, USA, 2017.
39. Crespi, P.; Zucca, M.; Valente, M. On the collapse evaluation of existing RC bridges exposed to corrosion under horizontal loads. *Eng. Fail. Anal.* **2020**, *116*, 104727. [CrossRef]
40. *CSI Bridge*; v18.2.0; Bridge Analysis, Desing and Rating. Computers and Structures Inc.: Walnut Creek, CA, USA, 2016. Available online: https://www.csiamerica.com/products/csibridge (accessed on 15 October 2016).
41. PEER; Pacific Earthquake Engineering Research Center. Strong Motion Database. 2014. Available online: https://ngawest2.berkeley.edu/ (accessed on 10 May 2022).
42. Koval, V.; Christopoulos, C.; Tremblay, R. Improvements to the simplified analysis method for the design of seismically isolated bridges in CSA-S6-14. *Can. J. Civ. Eng.* **2016**, *43*, 897–907. [CrossRef]
43. Rasouli, M.; Shiravand, M.R.; Ardakani, R.R. Substructure Mass Participation Effect on the Performance-Based Seismic Design Method for Isolated Bridges. *J. Bridge Eng.* **2023**, *28*, 04023095. [CrossRef]

Disclaimer/Publisher's Note: The statements, opinions and data contained in all publications are solely those of the individual author(s) and contributor(s) and not of MDPI and/or the editor(s). MDPI and/or the editor(s) disclaim responsibility for any injury to people or property resulting from any ideas, methods, instructions or products referred to in the content.